Prediction and minimization of NO$_x$ emission in a circulating fluidized bed combustor

Ke, Xiwei; Engblom, Markus; Yang, Hairui; Brink, Anders; Lyu, Jun Fu; Zhang, Man; Zhao, Bing

Prediction and Minimization of NO_x Emission in a Circulating Fluidized Bed Combustor: A Comprehensive Mathematical Model for CFB Combustion

Xiwei Ke[a], Markus Engblom[b], Hairui Yang[a], Anders Brink[b], JunFu Lyu[a], Man Zhang[a, *], Bing Zhao[c]

[a] State Key Laboratory of Power Systems, Department of Energy and Power Engineering, Tsinghua University, Beijing 100089, China

[b] Process Chemistry Centre, Åbo Akademi University, Biskopsgatan 8, 20500 Turku, Finland

[c] Huadian International Power Co., Ltd., Tianjin, 300280, China

Abstract

A comprehensive 1-dimensional/1.5-dimensional hybrid mathematical model is developed for predicting NO_x emission of a circulating fluidized bed (CFB) combustor under broader operating parameters. In this model, the local gas-solid fluidization state and gas/heat transfer conditions in different regions of a CFB combustor are specifically considered. Some two- or three-dimensional problems, such as bubble breakage over dense bed surface, secondary air injection, core-annular flow structure, and particle clusters in freeboard, are also taken into account in 1-D/1.5-D modeling. The detailed chemical kinetic mechanism is creatively used to describe the homogeneous reaction system towards CFB combustion simulation. In addition to operating parameters and fuel-specific inputs, no other model parameters can be trimmed from case to case. This integral CFB model is validated against the field test data obtained from three commercial CFB boilers with different capacities, some of which are first disclosed. Favorable comparisons are obtained between the predicted and measured results, involving particle size distributions, temperature and pressure profiles, and NO_x/SO_2 emissions. The final NO emission, as well as gas profiles, are somewhat different among the cases, which may be attributed to the discrepancy in boiler structure, fuel properties, and operating conditions. Further sensitivity analysis indicates that the proportion of volatile-N in total fuel-N, char combustion reactivity, and char-NO reactivity significantly impact the NO_x emission for CFB

25 combustion. Meanwhile, the gas-solid fluidization state also plays an essential role in the NO_x

26 emission and the in-furnace combustion efficiency, such as the gas flow distribution between phases,

27 bubble size, secondary air penetration depth, etc. However, the NO_x emission seems insensitive to

28 the particle external gas mass transfer coefficients.

29 **Keywords:** circulating fluidized bed; combustion; NO_x emission; mathematical model; validation

30 **Introduction**

31 Circulating fluidized bed (CFB) combustor has the advantages in fuel flexibility, good load

32 capability, and prominent de-NOx potentiality [1, 2]. However, with the increasing requirement of

33 pollution reduction, in order to consolidate the advantage of low pollution emission of CFB

34 combustors, it is necessary to further analyze the influence of operating parameters on NO_x emission

35 and deeply explore the low nitrogen combustion potential of CFB so as to promote clean and efficient

36 utilization of fossil fuel.

37 Research on the nitrogen chemistry in solid fuel-fired systems has been compiled in several

38 reviews [3-5]. Nevertheless, the complex nature of the two-phase flow, heat transfer and gas mixing

39 processes make the NO_x emission characteristic of a CFB combustor much more complicated.

40 Industrial practices have shown that the NO_x emission is not merely dependent on the fuel type but

41 also closely related to the combustor performance and operation conditions, e.g., temperature [6-8],

42 air staging degree [9-11], limestone addition [12, 13], bed quality [14], etc. However, carrying out

43 comprehensive field tests in industrial scale combustors is laborious and complex, sometimes even

44 impossible. By contrast, systematically applying the simulation method to investigate this issue is

45 more helpful in finding the optimum combination of the operating parameters to minimize pollutant

46　emissions. Therefore, in order to provide valuable engineering practice guidance and quantify the

47　NO_x emission process, a comprehensive CFB combustion model is required.

48　　　In most studies, the nitrogen chemistry for CFB combustion was generally described by limited

49　overall reactions (6~20 species and 3~20 steps) [15-20]. While no simplified mechanism is available

50　for all simulation conditions. For example, in the varying atmosphere, the conversion rate of HCN or

51　NH_3 to NO_x may be far different due to complex radical reactions [21-23]. Thus, a rigorous reaction

52　mechanism with sufficient reactants is necessary to describe homogeneous chemistry [24]. Other than

53　that, the heterogeneous or catalytic reactions over bed materials are of significance concerning their

54　possible role in reducing (char/ash) [25-27] or increasing (lime) [14, 28, 29] NO_x emission. In

55　addition, for an accurate description of the heterogeneous reaction rate, the transport phenomena in

56　both gas-solid two-phase flow and pore system of particles must be considered [30-33].

57　　　If applying the comprehensive description of homogeneous, heterogeneous, and catalytic

58　chemistry in modeling CFB combustion, the fluid dynamics of a CFB combustor need to be vastly

59　simplified considering computational restrictions. Moreover, the detailed information about gas-solid

60　turbulent flow is sometimes unnecessary in engineering. Therefore, a semi-empirical 1-dimensional

61　(1-D)/1.5-dimensional (1.5-D) representation of fluid dynamics has been preferred in many

62　engineering calculations [19, 34-37], which aim to include all phenomena that consider the effects of

63　the same or greater order of magnitude as the chemistry models. It is widely accepted that the flow

64　pattern in a CFB combustor is combined by a dense bed at the bottom and a dilute phase in the upper

65　furnace [38-40]. The bottom bed is often operated in a bubbling fluidization regime [38, 39], of which

66　a two-phase flow description in modeling is necessary [41-43]. While, the fluidization state in the

67   upper furnace can be a fast bed [1, 38] or pneumatic transport [39], where the internal solid

68   recirculation and cluster behavior should be reflected in simulation [44-46].

69   The gas mixing behavior in the splash zone is often neglected, while it has a significant impact

70   on the redox atmosphere formation, which is influenced by the bubble breakage and secondary air

71   (SA) injection. Lyngfelt et al. observed strong fluctuations between oxidizing and reducing conditions

72   above dense bed [47]. They pointed out that the gas from jets bypassing the bottom bed disintegrates

73   slowly over a specific distance. Namely, the O_2-rich gases are not instantaneously fully mixed over

74   the cross-section in the splash zone. In addition, due to the high solid suspension density, the

75   secondary air does not mix well with the upward gas stream, especially for the large-scale CFB boiler

76   [48, 49]. Therefore, it is a non-negligible problem to describe the gas mixing behavior in the splash

77   zone for 1-D/1.5-D CFB modeling.

78   The main objective of this work is to establish a comprehensive mathematical model that can

79   quantify the influence of fuel properties and operating conditions on NO_x emission. During this work,

80   the main sub-models and equations of the pseudo-steady-state 1-D/1.5-D hybrid CFB combustion

81   model are introduced, involving hydrodynamics (material balance), chemical reactions (energy

82   balance), and heat transfer (energy balance). These sub-models are inter-connected and solved

83   simultaneously by a FORTRAN code. The integral CFB model is validated against the field test data

84   obtained from three commercial CFB boilers with different capacities, one 135 MW_e super-high

85   pressure CFB boiler burning bituminous coal (BD-135), one 350 MW_e supercritical CFB boiler

86   burning bituminous coal (HP-350), and one 550 MW_e ultra-supercritical CFB boiler burning

87   Indonesian lignite (SC-550). A sensitivity analysis is also conducted to examine the effects of some

4

88 model parameters on the calculation results, involving heterogeneous reaction kinetics, fluid dynamic

89 parameters, and gas mass transfer coefficients.

2. Model description

2.1 Model structure

92   A schematic drawing of a CFB combustor (left) and the simplified modeling structure (right) are

93 shown in Fig.1. Each zone in the combustor riser is further divided into several cells (cyclones are

94 treated as one cell). Table.S1 in the supplementary material (SM) lists the model parameters

95 concerning the divisions of the cell, particle size, and particle age.
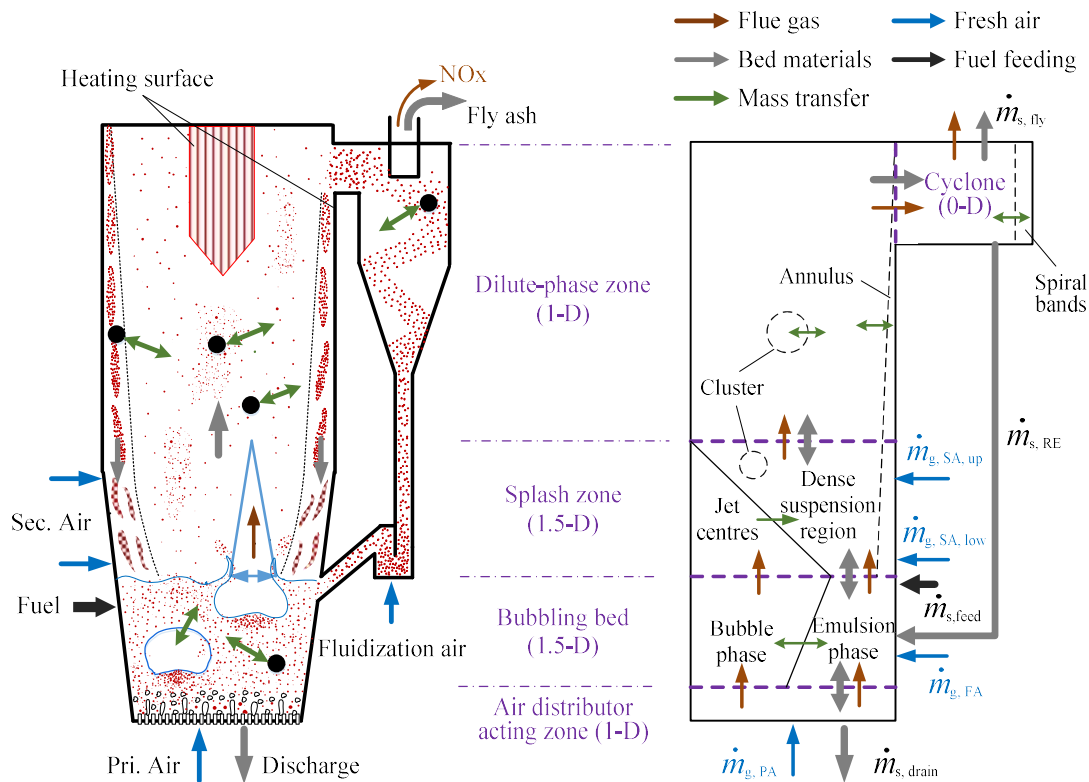
Fig.1   Schematics of the CFB combustor (left) and 1-D/1.5-D hybrid CFB model (right)

98   The CFB combustor is divided into five different zones according to the fluid dynamic and mass

99 transfer characteristics:

5

- The very bottom area is affected by the air distributors, where the rising bubbles are not fully developed. Considering the perturbation of jets from nozzles, the gas-solid in the air distributor acting zone is considered well-mixed.

- As the merger and growth of bubbles, the bubbling bed behavior becomes distinguished, and the region is gradually divided into bubble phase and emulsion phase. Cui et al. found that the voidage in bubbles is very close to unit [50]. Namely, all solids are in the emulsion phase.

- On the surface of the dense bed, bubbles burst, and the internal gas injects into the upper freeboard, which can be regarded as several parallel jets (bubble jet). The present model divides the splash zone into a particle-free high-velocity region (jet centers) and a dense, slower suspension region. The gas from the jets mixes gradually into the surrounding suspension over a specific height, whereas the gas concentration in the jet centers is not affected by the surroundings.

- The core-annular internal recirculation flow structure is observed above the dense bed [51, 52], and some particles in the core region can cluster [53, 54]. Hence the bed materials, including reactive fuel/lime particles, are divided into three parts: annulus, clusters, and single particles.

- Many particles inside cyclones are agglomerated into spiral bands moving along the wall, while the cluster behavior is not evident in the central region, and other solids are considered as single particles. The mass transfer of gas to spiral bands is similar to that in the riser annulus.

The integral CFB combustion model developed in this paper consists of three main modules: material balance (fluid dynamics), reactant balance (chemical reactions), and energy balance (heat transfer). The input scheme and main steps of the numerical solution are shown in Fig.2. Table.S1, (SM) lists the model parameters concerning the divisions of the cell, particle size, and particle age.
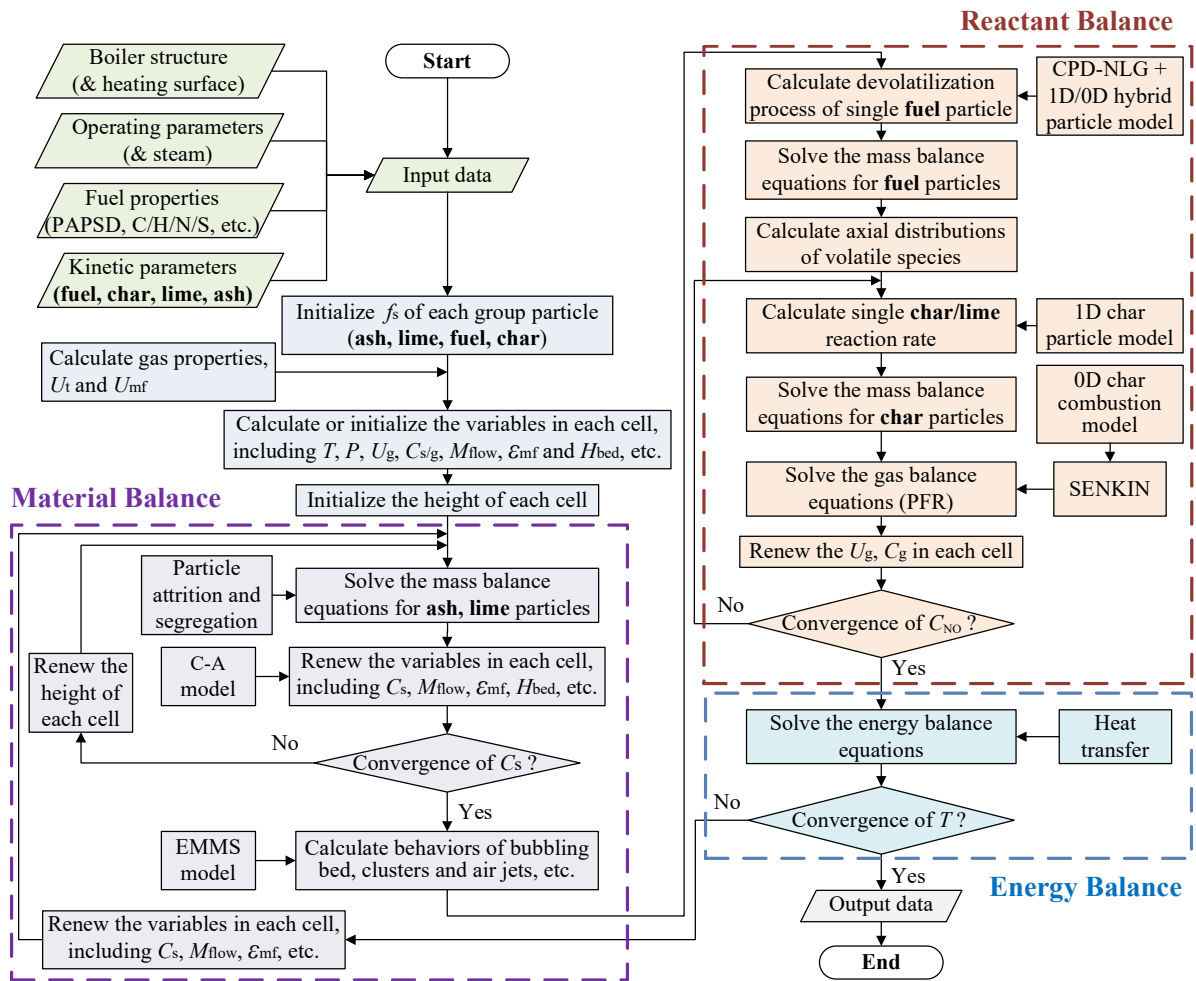
Fig.2 Flow chart of the numerical solution of the CFB combustion model

For the material balance and energy balance calculation, the one-dimensional back-flow description is adopted for the whole loop, that is, the interphase solids and heat transfer are ignored. In contrast, a two-phase model structure is used for gas balance in bubbling bed and splash zones (1.5-D description). The bubbles and the bubble jets are treated as pure gas channels based on the above analysis. Some literature also considers a particle-rich annulus and a particle-lean core region in upper zones for gas-phase calculation [42, 43]. Nevertheless, the thickness of the annulus is far smaller (0.1m ~ 0.18m [55]) than the industrial combustor size, and the gas velocity in the annulus is lower than that in the core region because of the wall friction [56]. Thus the reaction in the annular region may contribute a little to the total gas variation. In order to reduce the calculation time, the gas

132 phase in the upper zones is not further divided (1-D description). While the influence of core-annulus

133 flow is reflected in the heterogeneous reaction rate by estimating the mass transfer resistance of gas

134 from mainstream to annulus. Besides, the gas mass exchange between dispersed phase and clusters

135 is also considered.

136   Several sub-models have been introduced in previous studies [57, 58], involving material

137 balance, coal devolatilization, char combustion, lime sulphation, etc. However, some significant

138 modifications should be made to integrate them into the CFB combustion model of this work. In

139 particular, the chemical reactions and the gas balance calculation are re-established in this paper,

140 aiming to describe better the atmosphere variation and NOx formation in a CFB combustor.

141 *2.2 Hydrodynamics and material balance (1-D)*

142   All particles in each cell (i), involving ash, lime, fuel, and char, are specified with size (j) and

143 residence time (k) [57]. The mass balance of each category of solids is expressed as:

$$
\begin{aligned}
&\dot{m}_{s,\text{feed}(i,j,k=1)} + \dot{m}_{s,\text{RE}(i,j,k)} - \dot{m}_{s,\text{drain}(i=N_{\text{bot}},j,k)} - \dot{m}_{s,\text{fly}(i=1,j,k)} + \dot{m}_{s,\text{up}(i+1,j,k)} + \dot{m}_{s,\text{down}(i-1,j,k)} \\
&- \dot{m}_{s,\text{up}(i,j,k)} - \dot{m}_{s,\text{down}(i,j,k)} \left(+\dot{m}_{s,\text{shift}(i,j,k)} \right)\left(\pm \dot{m}_{s,r(i,j,k)} \right) + \dot{m}_{s(k-1)\rightarrow(k)} - \dot{m}_{s(k)\rightarrow(k+1)} = 0
\end{aligned}
\tag{1}
$$

144

145   A description of the items in Eq.(1) except $\dot{m}_{s,r}$ is listed in Table 1. $\dot{m}_{s,r}$ denotes the mass

146 change due to sulphation of CaO (mass increase), reductive decomposition of $CaSO_4$ (mass decrease),

147 fuel devolatilization (mass decrease), or char combustion (mass decrease), which will be described in

148 Section 2.3. Some basic hydrodynamic parameters are listed in Table.S2 (SM), which are used in the

149 calculations of material balance and mass transfer.

150   **Table 1   Determination of items in material balance equation Eq. (1)[i]**

Items	Determination		
Feed flow rate ($\dot{m}_{s,\text{feed}}$)	Solids	Primary particle size distribution $y_{\text{feed}(j,k=1)}$	Primary axial distribution $\psi_{\text{feed}(i,k=1)}$

Ash	Determined by SCCS experiment (PAPSD) [59][ii]	Calculated by burn-out char particle distribution
Lime	Feeding PSD	Limestone inlet
Fuel	Feeding PSD (hard fuel) or PAPSD (soft fuel) [57]	Fuel inlet
Char	PAPSD	Calculated by pyrolytic fuel particle distribution

Re-circulating mass flux	$\dot{m}_{s,\text{return}(i,j,k)} = \dot{m}_{s,\text{down}(i=1,j,k)}\psi_{\text{return}(i)}$
Discharge mass flux	$\dot{m}_{s,\text{drain}(i=N_{\text{bot}},j,k)} = \dot{m}_{s,\text{down}(i=N_{\text{bot}},j,k)}$
Fly ash mass flux	$\dot{m}_{s,\text{fly}(i,j,k)} = \dot{m}_{s,\text{up}(i=2,j,k)}\left(1-\eta_{\text{cyc}(j)}\right)$ [60]
Upward mass flux	$\dot{m}_{s,\text{up}(i,j,k)} = W_{s,\text{up}(i)} \cdot f_{s(i,j,k)} \cdot \xi_{(i,j)}$
Downward mass flux	$\dot{m}_{s,\text{down}(i,j,k)} = W_{s,\text{down}(i)} \cdot f_{s(i,j,k)}$
Mass flux caused by particle attrition[iii]	$\dot{m}_{s,\text{shift}(i,j,k)} = \dot{m}_{\text{fines}(i,j,k)} - \dot{m}_{\text{abra}(i,j,k)} + \dot{m}_{\text{redu}(i,j+1,k)} - \dot{m}_{\text{redu}(i,j,k)}$ [57, 58]
Age decline of particles	$\dot{m}_{s(k)\to(k+1)} = M_{s(i)}f_{s(i,j,k)} / \left(t_{(k+1)} - t_{(k)}\right)$
Complementary equation[iv]	$\sum\limits_{j=1}^{N_{j,A}}\sum\limits_{k=1}^{N_{t,A}} f_{\text{Ash}(i,j,k)} + \sum\limits_{j=1}^{N_{j,L}}\sum\limits_{k=1}^{N_{t,L}} f_{\text{Lime}(i,j,k)} = 1.0$ (for each cell i)

151 (i) η_{cyc} denotes the cyclone separation efficiency; $W_{s,\text{up}}$ and $W_{s,\text{down}}$ represent the total upward and downward solid

152 flux, respectively; $f_{s(i,j,k)}$ is the mass fraction of particles in (i, j, k) group; ξ denotes the segregation index; $\dot{m}_{\text{fines}}$

153 denotes fine particles generated by abrasion; $\dot{m}_{\text{abra}}$ denotes mass flux caused by abrasion; $\dot{m}_{\text{redu}}$ denotes mass flux

154 caused by reduction; $M_{s(i)}$ is the mass holdup in cell i.

155 (ii) The primary fragmentation of large fuel particles are considered, and the PAPSD is modified based on the model

156 proposed in Ref. [61]

157 (iii) The attrition of fuel and char particles is neglected due to the short time of devolatilization or combustion

158 process.

159 (iv) The mass balance calculation of fuel/char particles is decoupled from that of ash/lime particles (as shown in

160 Fig.2), namely, fuel and char particles are considered to flow with the primary bed materials (ash and lime) and

161 have little influence on the total material balance of a CFB combustor.

162   The two-region model proposed by Bai et al. is applied to describe the core-annular flow

163 structure in the freeboard zone and determine the upward mass flux (C-A model) [62]. Table.S3 (SM)

164 lists the intrinsic equations of this sub-model, including five independent equations, one optimization

165 condition, four equality constraints, and seven unknown variables (thickness of annulus (δ_a), mean

166 voidage in annulus or core region (ε_a, ε_c), mean gas velocity in annulus or core region ($U_{g,a}$, $U_{g,c}$),

167 mean particle velocity in annulus or core region ($U_{p,a}$, $U_{p,c}$)). For obtaining high computational

168   efficiency, this paper uses the simulated annealing algorithm [63] to solve the nonlinear optimization

169   problem of the C-A model.

170   Characteristics of clusters formed in the core region are described by the Energy-Minimization

171   Multi-Scale (EMMS) theory model [64, 65]. The original EMMS model consists of six independent

172   equations but having eight unknown variables (voidage in dilute phase or cluster ($\varepsilon_{c,f}$, $\varepsilon_{c,cl}$), superficial

173   particle velocity in dilute phase or cluster ($U_{p,f}$, $U_{p,cl}$), superficial gas velocity in dilute phase or cluster

174   ($U_{g,f}$, $U_{g,cl}$), cluster fraction (β_{cl}) and cluster diameter (d_{cl})). In order to avoid solving the time-

175   consumed nonlinear optimization problem, in this paper, two additional correlations are introduced

176   to close the equations. Table.S4 (SM) lists the intrinsic equations and the numerical solution steps of

177   the modified EMMS model.

178   *2.3 Chemical reactions and gas balance (1-D/1.5-D)*

179   Each cell is treated as a plug flow reactor (PFR) filled with evenly distributed solid materials,

180   whereas the bubbling bed zone and the splash zone consist of two parallel PFRs considering

181   interphase gas mass transfer (as shown in Fig.1). The division of cells listed in Table.S1 is rough for

182   gas balance calculation. Owing to the fast radical reaction rates, the gas residence time in such large

183   cells is too long to capture the variation of gas concentration gradients. For improving the calculation

184   accuracy, each cell is further divided into a series of sub-PFRs, and the gas residence time in these

185   sub-PFRs should be lower than a particular limit (as listed in Table.S1).

186   The gas balance for gaseous species *m* in sub-PFR *k* is expressed as follows:

187
$$U_{g(k)}C_{g(k,m)}A_{fur(k)} = \dot{m}_{g,in(k,m)}\left(+\dot{m}_{g,tran(k,m)}\right) + U_{g(k+1)}C_{g(k+1,m)}A_{fur(k+1)} + \sum R_{(k,m)} \quad (2)$$

10

188 where $\dot{m}_{\text{g,in}}$ denotes the injected gas flow rate, including fresh air and volatiles (all in particle phase);

189 $\dot{m}_{\text{g,tran}}$ denotes the interphase gas transport (only valid for bubbling bed and splash zone); A_{fur} is the

190 cross-sectional area in the furnace; U_{g} represents the gas velocity; C_{g} is the gas concentration; R

191 denotes the chemical reaction rates.

2.3.1 Kinetic models

193 Table.S5 (SM) lists the set of reactions and their kinetics used in this paper. Other than the

194 descriptions in previous studies [57, 58, 66], some contents necessitate further clarification.

195 • Fuel devolatilization.

196 The specific composition of volatile-nitrogen was not mentioned before. In this paper, all

197 volatile-N are considered as HCN or NH_3 [67, 68]. The yield of total volatile-N and the molar ratio

198 between HCN and NH_3 are related to the fuel type and temperature conditions [69, 70]. The fuel

199 devolatilization process is described by a developed 0D/1D hybrid particle model embedded with the

200 CPD-NLG model, while the chemical kinetic parameters about fast nitrogen release can be obtained

201 by the lab-scale bubbling fluidized bed experiments [66].

202 • Homogeneous reactions.

203 The detailed chemical kinetic mechanism, ÅA mechanism, which consists of 86 chemical

204 components and 522 elementary steps, is applied to describe the gas-phase chemistry [21]. The rates

205 of homogeneous reactions are calculated with the SENKIN reactor model in each control volume

206 (PFRs) [71]. Inputs to SENKIN are pressure, temperature, initial gas concentration, and gas residence

207 time, and as output SENKIN yields the concentrations at the outlet of a PFR. The gas velocity, as

208 well as residence time of each PFR, should be renewed during iteration since the total molar flow rate

209 may significantly change, especially in the bottom furnace.

210   In this work, except for char-nitrogen conversion, the heterogeneous reaction rate expressions

211   are also embedded in the SENKIN model and calculated with homogeneous reactions simultaneously

212   by the DASAC solver. The net conversion rate of char-N to NO ($X_{\text{char-N}}$) is determined by the 1D

213   particle model, which is computationally heavy (see the next section). Thus, this sub-model is solved

214   outside the gas balance calculation, and the $X_{\text{char-N}}$ is set as an iterative parameter. Besides, the

215   quenching and recombination of some radicals on the solid surface are of significance under fluidized

216   bed conditions, especially for the oxidation of reductive gas (like CO, CH_4) and homogeneous

217   nitrogen conversion [24, 72]. The recombination of four free radicals on the particle surface is

218   considered, as listed in Table.S5 (SM). The radical removal rate can be expressed by [72, 73]:

219
$$R_{(m)} = K_{\text{g}(m)}\gamma_{(m)}f_{\text{s}}\alpha_{\text{S/V}}C_{\text{g}(m)}, \quad m = \text{O}, \text{H}, \text{N}, \text{OH} \tag{3}$$

220   where K_{g} is the external mass transfer coefficient; f_{s} is the roughness factor for solids; $\alpha_{\text{S/V}}$ denotes

221   the collision cross-section per unit volume; γ is the recombination efficiency which gives the

222   probability that a radical recombines.

223   • Char reactions.

224   In this paper, the char reactions are described by two different particle models. For the char

225   combustion, CO_2/H_2O gasification, and reduction of surrounding NO, the single reaction rate

226   expressions (0D particle model) [58] are applied, which are embedded in the SENKIN model. While,

227   for the conversion of char-N, the NO formed inside char may continue to react with carbon and the

228    $X_{\text{char-N}}$ on the particle surface is significantly smaller than unit, which means the $X_{\text{char-N}}$ is strongly

229   affected by the particle size. Hence, the 1D spherically isothermal particle model should be

230   established to consider the char-N conversion. Totally six reaction steps (R7~R12) are involved here,

231   assumed to be at the pseudo steady state. For each time step and each component inside the particle,

232   the governing material balance equation is expressed as follow:

233
$$D_{e(m)}\left(\frac{d^2C_{g(m)}}{dr^2}+\frac{2}{r}\frac{dC_{g(m)}}{dr}\right)+\sum R_{(m)}=0, \quad m=O_2, CO_2, CO, H_2O, NO \tag{4}$$

234   where r is the radial position. D_e denotes the effective pore diffusion coefficient, which is the same

235   as that in the 0D particle model [58].

236   The boundary condition is:

237
$$\begin{cases} \left.\frac{dC_{g(m)}}{dr}\right|_{r=0}=0 \\ \left.D_{e(m)}\frac{dC_{g(m)}}{dr}\right|_{r=r_C}=K_{g(m)}\left(C_{g,\infty(m)}-C_{g,0(m)}\right) \end{cases} \tag{5}$$

238   The above five ordinary differential equations for chemical species are solved simultaneously

239   using the finite difference method. The $X_{\text{char-N}}$ is accordingly determined by calculating the

240   concentration gradient near particle surface:

241
$$X_{\text{char}-N}=\frac{D_{e,NO}\left.\frac{dC_{g,NO}}{dr}\right|_{r=r_C}}{\alpha_{N/C}\left(D_{e,CO}\left.\frac{dC_{g,CO}}{dr}\right|_{r=r_C}+D_{e,CO_2}\left.\frac{dC_{g,CO_2}}{dr}\right|_{r=r_C}\right)} \tag{6}$$

242   where $\alpha_{N/C}$ denotes the molar ratio of nitrogen to carbon in char.

243   • Catalytic reactions.

244   Four catalytic reactions on CaO particle surface are considered: the catalytic oxidation of CO

245   (R14) and NH_3 (R15), the hydrolysis of HCN (R16), and the reduction of NO by CO (R17).

246   Nevertheless, the sulphation product $CaSO_4$ is less active than CaO for these reactions [5]. Therefore,

247   the effective surface area for catalytic reaction can be expressed as:

248
$$s_{\text{CaO,e}(j,k)} = \frac{\text{MW}_{\text{CaO}}\left(X_{\text{CaO,max}(j)} - X_{\text{CaO}(j,k)}\right)}{X_{\text{CaO}(j,k)}\text{MW}_{\text{CaSO}_4} + \left(1 - X_{\text{CaO}(j,k)}\right)\text{MW}_{\text{CaO}}} s_{\text{CaO,ini}}$$ (7)

249   where $s_{\text{CaO,e}}$ and $s_{\text{CaO,ini}}$ are the effective specific area and initial specific area of the lime particle,

250   respectively; $X_{\text{CaO}(j,m)}$ is the sulphation conversion rate of a lime particle with size j at time k; $X_{\text{CaO, max}}$

251   is the maximum sulphation conversion rate; MW denotes the molar mass.

252   The intraparticle diffusion resistance of lime and ash particles might affect the catalytic reaction

253   rates. The following effectiveness factor is applied to evaluate its influence:

254
$$\eta_{\text{p}} = \frac{1}{\phi_{\text{p}}}\left[\frac{1}{\tanh\left(3\phi_{\text{p}}\right)} - \frac{1}{3\phi_{\text{p}}}\right]$$ (8)

255   where Φ_{p} is the Thiele modulus of a spherical particle, which is related to the reaction rate, pore

256   structure, gas diffusion coefficient, and temperature. The detailed analysis of the intraparticle

257   diffusion is described in the study of Fu et al. [74]

258   *2.3.2 Gas mass transfer*

259   •   Interphase gas mass transfer

260   In the bubbling bed at the bottom furnace, gas can transport from emulsion phase to bubble phase

261   as the merger and growth of bubbles. While for the splash zone, gas from the jet center mixes

262   gradually into the surrounding particle phase. These two gas transport phenomena are expressed as:

263
$$\dot{m}_{\text{g,tran}(k,m)}\big|_{\text{E}\to\text{B}} = \left[U_{\text{g,E}(k)}\left(1 - \sigma_{\text{B}(k+1)}\right)A_{\text{fur}(k+1)} - U_{\text{g,E}(k)}\left(1 - \sigma_{\text{B}(k)}\right)A_{\text{fur}(k)}\right]C_{\text{g,E}(k+1,m)}$$
$$\dot{m}_{\text{g,tran}(k,m)}\big|_{\text{J}\to\text{S}} = \left(U_{\text{g,J}(k+1)}\sigma_{\text{J}(k+1)}A_{\text{fur}(k+1)} - U_{\text{g,J}(k)}\sigma_{\text{J}(k)}A_{\text{fur}(k)}\right)C_{\text{g,J}(k+1,m)}$$ (9)

264   where the subscripts E, B, J, S denote emulsion phase, bubble phase (bubbling bed), jet center zone,

265   and jet surroundings (splash zone), respectively; σ is the volume fraction of pure gas phase.

14

266   Besides, the interphase gas mass transfer induced by concentration difference also exists in

267   bubbling fluidized bed:

$$\dot{m}_{g,\text{tran}(k,m)}\Big|_{B\leftrightarrow E} = K_{g,B\leftrightarrow E(k,m)}S_{B(k)}\left(C_{g,B(k,m)} - C_{g,E(k,m)}\right)$$

268
$$K_{g,B\leftrightarrow E(k,m)} = \frac{U_{\text{mf}(k)}}{3} + \left(\frac{4D_{g(k,m)}\varepsilon_{\text{mf}(k)}U_{g,B(k)}}{\pi d_{B(k)}}\right)^{1/2} \tag{10}$$

269   where $K_{g,B\leftrightarrow E}$ denotes the interphase gas mass transfer coefficient [75]; S_B is the surface area of

270   bubbles; d_B is the bubble diameter; $U_{g,B}$ is the bubble rising velocity; U_{mf} is the minimum fluidization

271   velocity; D_g is the molecular gas diffusivity; ε_{mf} is the minimum fluidization voidage.

272   • External mass transfer (except for annular region)

273   The external mass transfer around active particles (char, lime, or ash) is expressed as:

274
$$R_{(m)} = K_g\left(C_{g,\infty(m)} - C_{g,S(m)}\right) \tag{11}$$

275   where $C_{g,\infty}$ and $C_{g,S}$ are the gas concentrations in ambiance and on the particle surface, respectively.

276   K_g is closely related to the local gas-solid fluidization state, which can be calculated by the following

277   semi-empirical correlations ($\text{Sh} = K_g d_p / D_g$, d_p is the particle size):

278   (1) In the emulsion phase in bubbling bed [76]:

279
$$\text{Sh}_E = 2\varepsilon_{\text{mf}} + 0.70\left(\frac{U_{\text{mf}}d_p\rho_g}{\mu_g\varepsilon_{\text{mf}}}\right)^{1/2}\left(\frac{\mu_g}{\rho_g D_g}\right)^{1/3} \tag{12}$$

280   (2) For single particles in upper zones [31]:

281
$$\text{Sh}_{\sin} = 2\varepsilon_{c,f} + 0.69\left(\frac{U_{ss,f}d_p\rho_g}{\mu_g}\right)^{1/2}\left(\frac{\mu_g}{\rho_g D_g}\right)^{1/3} \tag{13}$$

282   where $U_{ss,f}$ denotes the superficial slip velocity in the dilute phase.

283   (3) In the clusters in upper zones [31] (normally $\text{Sh}_E < \text{Sh}_{cl} < \text{Sh}_{\sin}$):

$$284 \qquad \mathrm{Sh_{cl}} = 2\varepsilon_{c,cl} + 0.69 \left(\frac{U_{ss,cl} d_p \rho_g}{\mu_g} \right)^{1/2} \left(\frac{\mu_g}{\rho_g D_g} \right)^{1/3} \qquad (14)$$

285   where $U_{ss,cl}$ is the superficial slip velocity in cluster.

286   •   External mass transfer in annular region

287   In this paper, the heterogeneous reactions in the annular regions (including the spiral bands in

288   cyclones) are treated as "sheath reaction", which is derived from the carbon group combustion theory

289   proposed by Annamalai et al. [77, 78]. While three main assumptions should be made: ⑴ the near-

290   wall particle cloud is simplified as a slab with the same thickness as annulus; ⑵ the near-wall

291   particle cloud is uniform and isothermal; ⑶ the mass transfer resistance from ambiance to annulus

292   surface is ignored. Hence, the group reaction number G' and the effective reaction coefficient of near-

293   wall active particles are expressed as [79]:

$$294 \qquad G' = \frac{\text{mass transfer between bulk gas and particles within annulus}}{\text{mass transfer between ambience and annulus surface}} = \frac{S_{V,p} \delta_a^2 \mathrm{Sh}_a / (f_p d_p)}{1 + \mathrm{Sh}_a D_g / (f_p R_{(m)} d_p)} \qquad (15)$$

$$295 \qquad \eta_{eff} = \frac{\text{reaction rate of particles inside annulus}}{\text{reaction rate of particles at annulus surface}} = \frac{\tanh \left[(G')^{1/2} \right]}{(G')^{1/2}} \qquad (16)$$

296   where $S_{V,p}$ denotes the surface area of active particles per unit volume; Sh_a is the Sherwood number

297   of a single particle in a cloud; f_p is the mass fraction of active particles in the annulus. The reaction

298   rates of particles at the annulus surface can be considered the same as that of single particles in the

299   dilute phase.

300   •   Gas mixing of secondary air

301   The SA jet usually deflects at a certain depth and flows parallelly with the mainstream;

302   meanwhile, the oxygen from the jet mixes gradually into the surroundings. The trajectory of SA is

303 similar to a quadratic curve. Yang et al. argue that the penetration depth of SA ($l_{SA,pene}$) corresponds

304 to the point where the deflection angle is about 80°, and propose an empirical correlation as follows

305 [80]:

$$\frac{l_{SA,pene}}{d_{SA,in}} = 1.7255 \left(\frac{\rho_{g,SA} U_{g,SA}^2}{\rho_{g,flue} \overline{U}_g^2 + \rho_p (1-\overline{\varepsilon}) \overline{U}_p^2} \right)^{0.5} \qquad (17)$$

307 where $d_{SA,in}$ is the diameter of SA inlet; $U_{g,SA}$ denotes the SA injection velocity; $\rho_{g,SA}$ and $\rho_{g,flue}$ are

308 the densities of SA and flue gas, respectively; $\overline{U}_g / \overline{U}_p$ denote the mean gas/particle velocity across

309 the furnace.

310   Wang et al propose an empirical correlation to describe the attenuation of gas concentration in

311 SA jet center [81], which is applied here to roughly estimate the distribution of oxygen in the cells

312 located SA inlets:

$$\frac{\dot{m}_{g,in(i=N_{SA},O_2)}}{\dot{m}_{O_2,SA}} = \exp\left(-0.66 \frac{0.5 d_{fur} - l_{SA,pene}}{d_{SA,in}} - 0.71 \right) \qquad (18)$$

314 where $\dot{m}_{O_2,SA}$ denotes the total oxygen inflow rate with SA; d_{fur} is the depth of the furnace.

315   The residual oxygen carried by SA is assumed to be linearly distributed over a certain height

316 ($H_{AS,J}$). Namely, when the SA jet reaches a certain axial position (assuming 80% of the radius of the

317 furnace), it cannot be distinguished from the mainstream, and the corresponding height is expressed

318 as:

$$H_{SA,J} = \frac{\tan(80°)}{2 l_{SA,pene}} \left(0.8 l_{mid,fur} \right)^2 + H_{SA,in} \qquad (19)$$

320 *2.4 Heat transfer and Energy balance (1-D)*

321   The energy balance of cell i is written as:

17

322
$$\begin{cases} \sum Q_{\text{in}(i)} - \sum Q_{\text{out}(i)} + \sum Q_{\text{r}(i)} - \sum Q_{\text{hs}(i)} = 0 \\ \sum Q_{\text{in}(i)} = Q_{\text{feed}(i)} + W_{\text{s,RE}(i)} h_{\text{s}(i=1)} + W_{\text{s,up}(i+1)} h_{\text{s}(i+1)} + W_{\text{s,down}(i-1)} h_{\text{s}(i-1)} + W_{\text{g,up}(i+1)} h_{\text{g}(i+1)} \\ \sum Q_{\text{out}(i)} = W_{\text{s,drain}(i=N_{\text{bot}})} h_{\text{s}(i=N_{\text{bot}})} + W_{\text{s,fly}(i=1)} h_{\text{s}(i=1)} + W_{\text{s,up}(i)} h_{\text{s}(i)} + W_{\text{s,down}(i)} h_{\text{s}(i)} + W_{\text{g,up}(i)} h_{\text{g}(i)} \end{cases} \quad (20)$$

323 where Q_{in} and Q_{out} denote the heat flow accompanied by the flow of solids and gas; Q_{feed} represents

324 the heat input from raw fuel and hot air; Q_{r} denotes the reaction heat; Q_{hs} denotes the heat adsorbed

325 by heating surface. h_{s} and h_{g} are the sensible enthalpies of solids and flue gas, respectively.

326   The heat transfer from bed to heating surface in a CFB boiler is affected by several factors:

327 heater configuration, flue gas velocity, gas properties, solid concentration near the wall, and bed

328 material properties. Lyu et al. [82] proposed a semi-empirical model to estimate the local heat transfer

329 coefficient, which has been used in the design of CFB boilers with a vast capacity:

330
$$Q_{\text{hs}} = K_{\text{h}} A_{\text{S,b}} \Delta T \quad (21)$$

331
$$\frac{1}{K_{\text{h}}} = \frac{1}{K_{\text{b}}^{n}} + \frac{1}{K_{\text{f}}} \frac{A_{\text{S,b}}}{A_{\text{S,f}}} + \frac{\delta_{\text{fin}}}{\lambda_{\text{fin}}} \left(+\frac{\delta_{\text{r}}}{\lambda_{\text{r}}} + \frac{1}{K_{\text{c}}} \right) \quad (22)$$

332 where K_{h} represents the total heat transfer coefficient; ΔT is the temperature difference between

333 furnace and working medium; K_{b}^{n} denotes the nominal heat transfer coefficient from bed to wall;

334 K_{f} denotes the heat transfer coefficient at working medium side; $A_{\text{S,b}}$ and $A_{\text{S,f}}$ are the heating surface

335 areas at flue gas side and working medium side, respectively; δ_{fin} and δ_{r} are the thicknesses of fin and

336 refractory castable, respectively; λ_{fin} and λ_{r} are the heat conductivities of steel cylinder and refractory

337 castable, respectively; K_{c} denotes the heat transfer coefficient of contamination on heating surface.

338 **3. Field tests**

339   The field test data from three different commercial CFB boilers are applied to validate the CFB

340 combustion model developed in this study, one 135 MW$_{\text{e}}$ super-high pressure CFB boiler (BD-135),

341   one 350 MW$_e$ supercritical CFB boiler (HP-350), and one 550 MW$_e$ ultra-supercritical CFB boiler

342   (SC-550). The main structure of these boilers and the layouts of some in-furnace pressure/temperature

343   measuring points are shown in Fig.S1 (SM). The BD-135 and SC-550 boilers have been described in

344   detail in previous studies [57, 58]. The HP-350 boiler is located in China, of which the main steam

345   pressure and main steam temperature under BMCR condition are 25.31 MPa and 571 °C, respectively.

346   Other than the low-NO$_x$ combustion and limestone in-situ desulphurization, the SNCR and WFGD

347   systems are also arranged to maintain the stable up-to-standard NO$_x$ and SO$_2$ emissions of this boiler.

348   The ultimate and proximate analysis of the fuels burned in the field tests is listed in Table 2. The

349   ash formation characteristics of these fuels, i.e., PAPSD matrixes and ash particle attrition rate

350   constants, are shown in Fig. S2 (SM).

351   **Table 2   The ultimate and proximate analysis of fuels**

Boiler	Fuel	Proximate analysis / %				Ultimate analysis / %					$Q_{ar,net,p}$ / MJ·kg^{-1}
		M_{ar}	A_{ar}	V_{ar}	FC_{ar}	C_{ar}	H_{ar}	O_{ar}	N_{ar}	S_{ar}	
BD-135	Bituminous 1	10.03	46.23	22.02	21.72	32.81	2.64	7.11	0.76	0.42	13.20
HP-350	Bituminous 2	6.51	42.53	16.66	34.30	40.81	2.51	4.98	0.36	2.29	14.50
SC-550	Lignite	24.94	5.33	34.35	35.38	50.25	3.97	14.34	0.83	0.34	20.20

352   The PSDs of feeding fuel and limestone are shown in Fig. S3 (SM). Some other main operating

353   parameters during the test are listed in Table 3. For the SC-550 CFB boiler, the heating surface

354   structure and working medium parameters are unavailable; namely, the heat transfer coefficient and

355   the in-furnace energy balance, cannot be calculated accurately. However, according to industrial

356   practice, the temperature inside a CFB boiler furnace is nearly uniform under high load conditions

357   [1, 38]. Hence the cells in the riser of this boiler can be roughly considered to have the same

358   temperature (simulation input).

Table 3　Main operating parameters of the three CFB boilers in field tests

Item		BD-135	HP-350	SC-550
Boiler load / MW		131	199.5	507.5
Coal feeding rate / kg·s⁻¹		28.0	36.9	69.3
Calcium sulphur ratio		2.8	2.5	2.5
Furnace pressure drop / kPa		4.5	7.5	5.0
Excess air coefficient		1.13	1.12	1.17
Primary air ratio* / %		50	55	60
Ratio of air from upper SA inlets / %		16	11	13
Ratio of air from lower SA inlets / %		16	21	15
Temperature of working medium / °C	Water wall (& water-cooled panel)	338	296~372	-
	Superheater (in-furnace)	391 to 481	429 to 502 (2nd) 482 to 551 (3rd)	-
	Reheater (in-furnace)	461 to 539	430 to 551	-

* The BD-135 CFB boiler also has middle SA inlets. Other than the primary air and secondary air, there are other air sources such as fluidization air below loop seal, air flowing with feeding coal, etc.

Field test results include the temperature/pressure axial profiles in the furnace; PSDs of fly ash sampled from fly ash silo, bottom ash sampled after slag cooler (BD-135 & HP-350) or from conveying belt (SC-550), and circulating ash sampled from loop seals (BD-135 & SC-550) or before cyclone inlets (HP-350); some gaseous species concentrations, etc. The gas concentrations were recorded from the Continuous Emission Monitoring System (CEMS) directly. The O_2 measuring points are set in the outlet of cyclones, while the NO_x emission values were taken from the measuring points set before the FGD tower (BD-135 & HP-350) or SCR reactor (SC-550); meanwhile, the SNCR systems were stopped during the tests.

4. Results and discussion

4.1 Model validation

The operating parameters of the field tests are used as the model input parameters for comparison. Meanwhile, the fuel properties vary from case to case, which should be obtained by specific

374 experiments, involving ultimate and proximate analysis, physical properties of fuel and char (like

375 particle density), ash formation characteristics (obtained by SCCS method), fuel devolatilization, and

376 char reaction kinetics (obtained by bubbling bed or fixed bed experiments, as listed in Table.S5 (SM)),

377 etc. Other built-in model parameters should be kept the same for different simulation cases. Namely,

378 when simulating a new combustor, in addition to operating parameters and fuel-specific input, no

379 other model parameters can be trimmed freely.

380 Some characteristic field test data, including the medium diameter (d(0.5)) of sampled ash,

381 unburned carbon content in fly or bottom ash, NO_x and SO_2 emissions, etc., are compared with the

382 simulation results, as listed in Table 4. It is seen that most simulation results for different CFB boilers

383 are in good agreement with the test results. Fig.3 and Fig.4 also show that the model satisfactorily

384 predicts the PSDs of bed materials, axial temperature profiles, and pressure drop distributions alone

385 furnace. It indicates that the mathematical CFB combustion model developed in this paper is reliable

386 to be applied to further study the effects of operating conditions on the pollutant emissions for a CFB

387 combustor.

388 **Table 4 Comparison of some simulation results with field test data**

| Item	BD-135		HP-350		SC-550	
	Model	Exp.	Model	Exp.	Model	Exp.
d(0.5) of fly ash / μm	53.5	48.7	32.3	46.8	16.2	15.6
d(0.5) of bottom ash / μm	578.9	-*	565.1	509.3	200.5	207.9
d(0.5) of circulating ash / μm	162.9	167.7	108.0	106.8	142.9	139.2
Mass flow ratio of fly ash to bottom ash	1.25	1.50	0.68	-	1.42	1.65
Carbon content in fly ash / %	3.56	3.22	1.74	1.89	2.77	2.71
Carbon content in bottom ash / %	1.65	1.81	2.69	2.44	0.77	0.68
C_{O2} in outlet of cyclone / %	2.65	2.60	2.53	2.45	3.07	3.08
C_{NOx} in outlet of cyclone / mg·Nm^{-3}	222	221	56	53	365	374
C_{SO2} in outlet of cyclone / mg·Nm^{-3}	421	-	1209	1124	61	56

389 * The relevant field test data were not obtained.
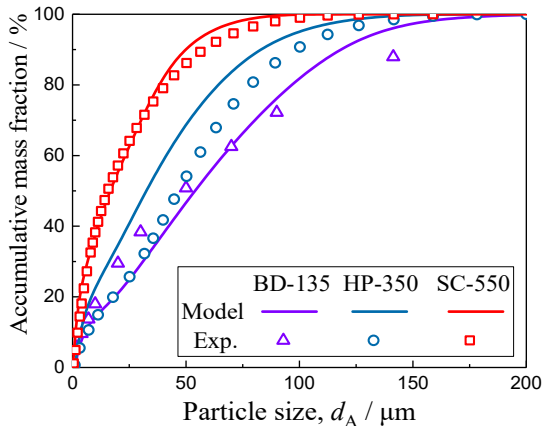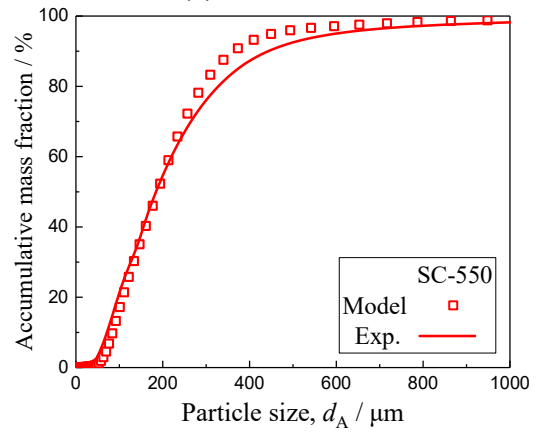
(a) Fly ash
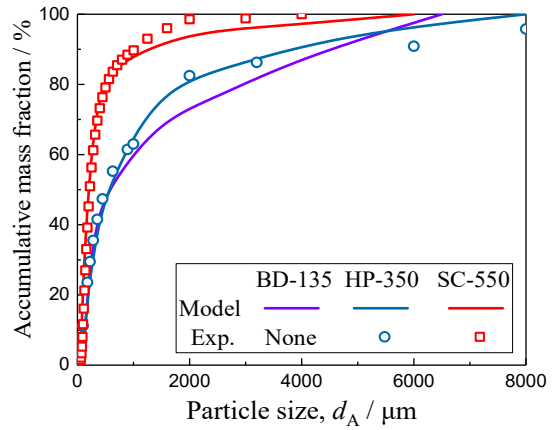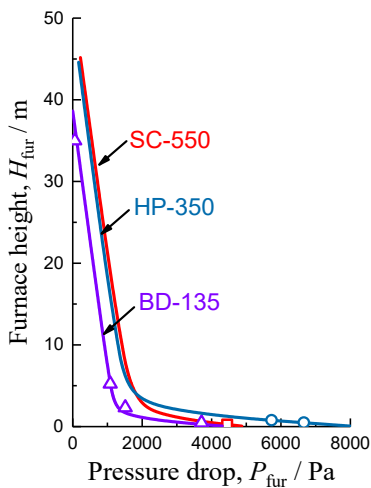
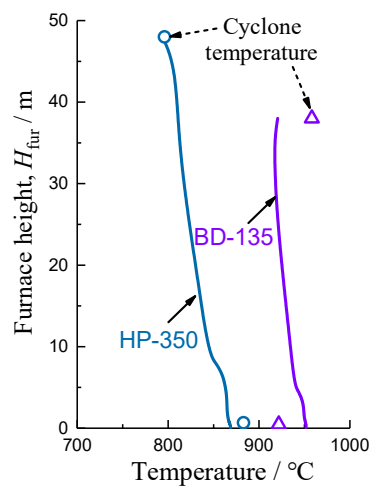**(b) Bottom ash**
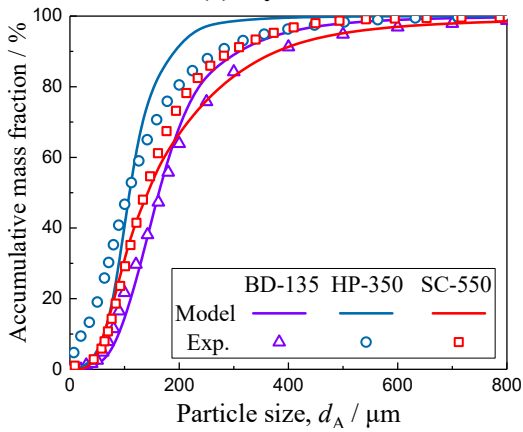
(c) Circulating ash

(d) INTREX ash (SC-550)

390   **Fig.3 Comparison of simulated ash particle size distributions with field test data**

(a) Bed pressure

(b) Temperature

391   **Fig.4 Comparison of simulated pressure and temperature profiles alone furnace with field test data**

392   **(Line: simulated value; point: field test data)**

393   *4.2 Comparison of three simulation cases*

394   The NO_x emission is significantly affected by many operation conditions of the CFB boiler. For

395   instance, the increase of primary air ratio or furnace temperature usually leads to an increase in NO_x

396   emission [6-11]. In addition, some studies have found that the NO_x emission of CFB combustors is

397   positively correlated with the fuel volatile content [83]. The SC-550 boiler adopted a high primary

398   air ratio (~60 %), and the furnace temperature of the BD-135 boiler was relatively high (~ 950 ℃).

399   Meanwhile, coals burned in these two boilers both have high volatile contents. Hence, the NO_x

400   emissions of the SC-550 boiler (374 mg·m^{-3}) and BD-135 boiler (221 mg·m^{-3}) were much higher than

401   the HP-135 boiler (53 mg·m^{-3}). In fact, NO_x emission characteristics for the CFB combustion are

402   much more complex than the above analysis. Any design or operating parameter adjustment, such as

403   cyclone efficiency, feeding coal or limestone size, etc., may lead to the difference in final NO_x

404   emission. More detailed analysis needs to be conducted in the future.

405   Fig.5 presents the simulated axial profiles of O_2, CO, and NO concentrations in different CFB

406   boilers. The results shown in these figures are the cross-sectional average gas concentration at a

407   corresponding height. For the bubbling bed and splash zone, the pure gas channels (bubble phase or

408   bubble jet centers) and particle-rich areas (emulsion phase or dense suspension region around bubble

409   jets) coexist. As shown in Fig.6, in the emulsion phase at the bubbling bed, the oxygen and nitric

410   oxide contents decrease significantly in height, while the CO concentration is pretty high. For the

411   bubble phase, due to the weak heterogeneous reactions, the gas concentration variation is much more

412   moderate. Since the gas compositions are different between the bubble phase and emulsion phase, an

413　alternative reducing and oxidizing atmosphere can be observed above the dense bed as the bubbles

414　burst.

(a) O₂　　　　　(b) CO　　　　　(c) NO
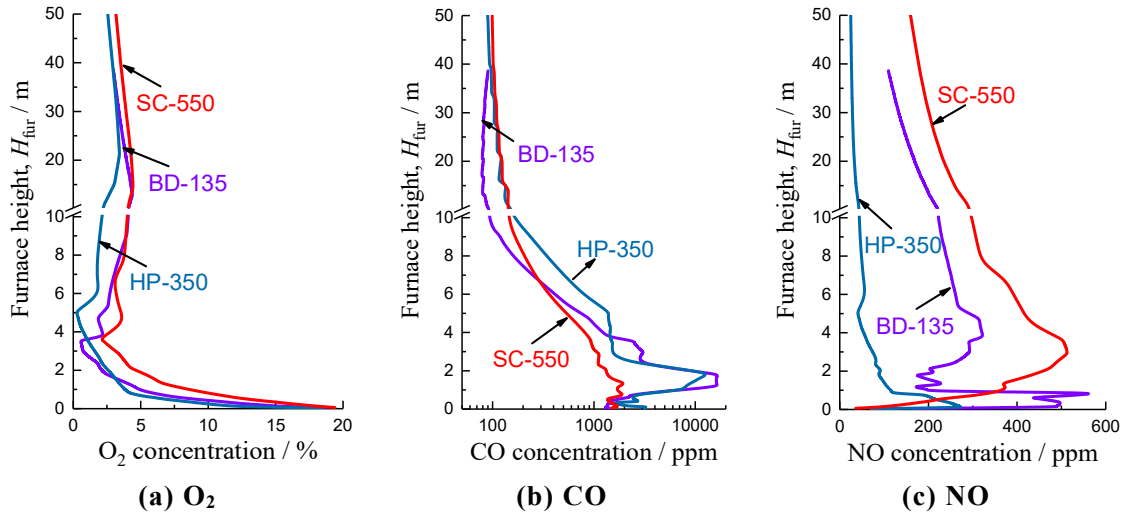
415　**Fig.5 The simulated axial profiles of O₂, CO, and NO concentration**

(a) O₂　　　　　(b) CO　　　　　(c) NO
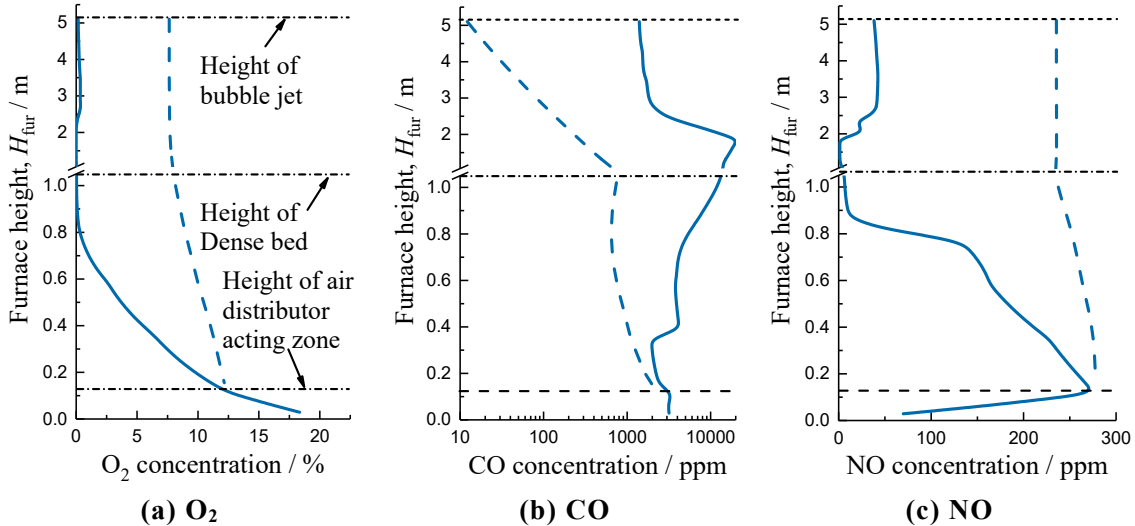
416　**Fig.6 The axial profiles of gas concentration in two-phase regions at the bottom furnace (HP-350)**
417　**(Solid line: particle-rich areas; dotted line: pure gas channels)**

418　　　　Fig.5(c) shows that large amounts of NO are generated in the lower part of the furnace, and the

419　peaks of C_{NO} profile are located in the air distributor acting zone (HP-350), above the dense bed

420　surface (BD-135) or near secondary air inlets (BD-135 & SC-550). The specific distribution form is

421　affected by many factors, e.g., fuel properties (especially volatile content), feeding coal PSD, layouts

422　of coal inlets and SA inlets, etc. For instance, due to the high volatile content and good fragmentation

24

423   and attrition performances, the Indonesian lignite has a fine primary particle size and a rapid

424   devolatilization rate. Hence, nearly 80% of total volatiles (volatile-N) in the SC-550 CFB boiler are

425   released near the coal inlets, as shown in Fig. S4(c) (SM). Meanwhile, the lower SA inlets are close

426   to the coal inlets in this boiler. Thus a large amount of NO is generated near the SA inlets, and a

427   unimodal distribution of NO concentration along furnace height is presented. However, for the BD-

428   135 CFB boiler, a considerable number of large coal particles stay in the bottom dense bed, and nearly

429   30% of volatiles are released here. The lower SA inlets are also close to the dense bed surface. In

430   addition to gas dilution, part of NO generated in the dense bed may be reduced by the volatile-N (such

431   as NH_3) released near coal inlets, leading to a rapid decrease of NO concentration above the dense

432   bed surface. While, for the higher region located upper SA inlets, some NO is generated due to the

433   continuous oxidation of char-N or volatile-N, and another NO concentration peak is formed.

434   Nevertheless, for all three cases, the C_{NO} gradually decreases in the upper furnace. It is because

435   almost all volatiles (-N) are released and wholly combusted in the bottom furnace, while the

436   heterogeneous reduction of NO (like char-NO reaction) becomes predominant in the dilute phase

437   zone. This trend has also been proved in many field tests [12, 84, 85].

438   Some other simulation results are given in the Fig. S4 ~ Fig. S8 (SM), including the residence

439   time of different size particles, axial distributions of voidage, mean particle size and volatiles, etc.

440   *4.3 Sensitivity analysis*

441   The integral CFB combustion model contains many parameters, including chemical kinetics,

442   gas-solid two-phase flow parameters (such as bubble size), gas mass transfer coefficients, heat

443   transfer coefficients, and model structure parameters (such as cell division), etc. The determination

444   of each parameter has discrepant effects on the simulation results.

445   Fig.7 shows the sensitivity of calculated final NO_x emission to some main heterogeneous

446   reaction kinetics, involving the ratio of HCN to NH_3 in volatile-N ($\alpha_{HCN/NH3}$), fast nitrogen release

447   kinetics (k_N, which is related to the distribution of fuel-N), char combustion reactivity (k_{C-O2}), char

448   CO_2 gasification reactivity (k_{C-CO2}), the ratio of CO to CO_2 in the products of char combustion (α_{C-}

449    $_{O2}$), char-NO reactivity (k_{C-NO}), catalytic reduction of NO on ash surface (k_{A-NO}), catalytic oxidation

450   of CO on CaO surface (k_{L-CO}), catalytic hydrolysis of HCN on CaO surface (k_{L-HCN}), catalytic

451   oxidation of NH_3 on CaO surface (k_{L-NH3}) and catalytic reduction of NO on CaO surface (k_{L-NO}).
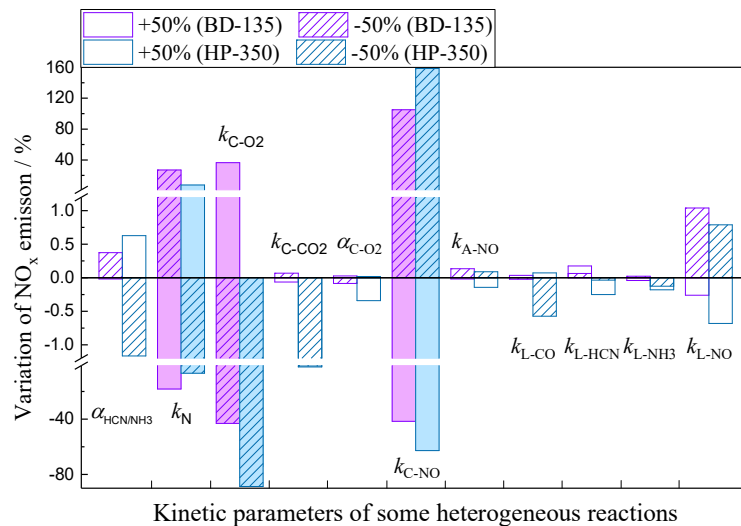

452
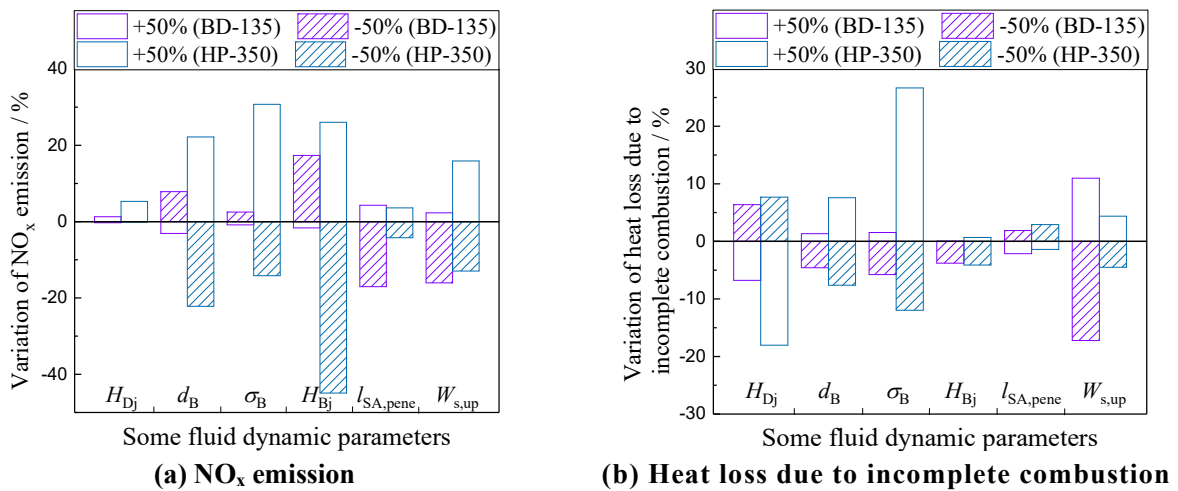453   **Fig.7 Sensitivity analysis of some heterogeneous reaction kinetics for the CFB model**

454   It indicates that k_N, k_{C-O2}, and k_{C-NO}, namely, the yield of volatile-N and char reactivities, have

455   significant impacts on the NO_x emission for CFB combustion, whereas these chemical kinetic

456   parameters are closely related to the fuel type. Hence, to ensure the reliability of model predictions,

457   it is better to determine these parameters for different kinds of fuel by separate experiments.

458   Fig.8 and Fig.9(a) show the sensitivity of calculated final NO_x emission to the gas mass transfer

459   coefficients and some fluid dynamic parameters, respectively. Fig.9(b) further illustrates the effects

26

460   of gas-solid fluidization state on the in-furnace combustion efficiency. In Fig.8, $K_{g,B\leftrightarrow E}$, $K_{g,E}$, G',

461     $K_{g,cl}$ and $K_{g,sin}$ denote interphase mass transfer coefficient between bubble phase and emulsion phase,

462   mass transfer coefficient in emulsion phase, group reaction number towards annular region (the mass

463   transfer resistance will be greater if G' become higher), mass transfer coefficient for clusters in core

464   region and mass transfer coefficient for single particles in core region. In Fig.9, H_{Dj}, d_B, σ_B, H_{Bj},

465     $l_{SA,pene}$ and $W_{s,up}$ denote penetration depth of jets from nozzles (height of air distributor acting zone),

466   bubble size, volume fraction of bubbles, length of jets induced by bubble breakage, penetration depth

467   of SA and total upward solid flow rate. Note that σ_B is only increased by 25% for avoiding $\sigma_B > 1$.
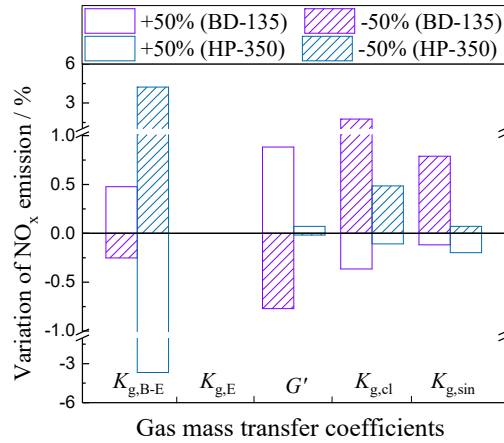
468
469   **Fig.8 Sensitivity analysis of gas mass transfer coefficients for the CFB model**

(a) NOₓ emission   **(b) Heat loss due to incomplete combustion**

470   **Fig.9 Sensitivity analysis of some fluid dynamic parameters for the CFB model**

471   The sensitivity analysis shows that the final NO_x emission seems insensitive to the particle

472   external gas mass transfer coefficients. However, the variation of the local gas-solid fluidization state

473   has significant effects on the combustion and NO_x emission. For instance, when the H_{Dj} is high (more

474   primary air or fewer nozzles), the contact between large fuel particles and oxygen in the bottom

475   furnace is sufficient, which contributes to reducing the char content in bottom ash and the heat loss.

476   While the reducing atmosphere is also weakened, and the NO_x emission may increase. Suppose the

477   solid suspension density in the splash zone increases or the secondary air inlet velocity decreases, the

478   $l_{SA,pene}$ generally decreases. In that case, the fresh oxygen diffusion will be difficult, resulting in an

479   enhanced reducing atmosphere in the upper furnace and a reduction in NO_x emission. Nevertheless,

480   combustion efficiency is inevitably affected.

481   All these sensitivity parameters are related to the operation conditions of a CFB combustor. The

482   adjustment of fuel properties, cyclone efficiency, feeding coal size, air staging, etc., usually leads to

483   simultaneous changes in the characteristics of local gas-solid two-phase flow, heat, and mass transfer,

484   which may have significant effects on the atmosphere or temperature distributions inside the furnace.

485   Consequently, the nitrogen-containing reactions' rate and the final NO_x emission are affected. For

486   this intricate nonlinear system, the effects of an operating parameter on various intermediate

487   processes may be discrepant, even opposite. Thus the presented variation trend of NO_x emission is

488   sometimes non-monotonous and unfixed. It brings many difficulties for the systematical analysis of

489   a CFB combustor and optimizing the operating conditions to minimize the pollution emission.

5. Conclusions

The paper has established a comprehensive 1-dimensional/1.5-dimensional hybrid mathematical model for CFB combustion, which integrates the chemical reaction, fluid dynamics, and heat transfer. Developed CPD-NLG devolatilization model and 0D/1D hybrid particle model are applied to describe fuel/char/lime reaction processes, as well as the heterogeneous nitrogen conversion. The particle age is introduced in modeling bed material balance, thereby considering the reaction state variation of active particles over time. Besides, a detailed chemical kinetic mechanism is necessary to calculate the homogeneous reactions. For the fluid dynamics in a CFB combustor, the local gas-solid fluidization state and gas/heat transfer conditions in different regions of a CFB combustor are fully taken into accounts, such as the agitation of nozzle jet near air distributor, bubbling behavior in the bottom bed, gas mixing caused by bubble breakage and secondary air injection in the splash zone, core-annular flow structure and cluster characteristics in freeboard.

This integral CFB combustion model is validated against the field test data obtained from three commercial CFB boilers, a 135 MW_e super-high pressure CFB boiler, a 350 MW_e supercritical CFB boiler, and a 550 MW_e ultra-supercritical CFB boiler, involving particle size distributions, furnace temperatures and pressures, pollutant emissions, etc. The final NO emission and gas profiles are somewhat different among the cases, which may be attributed to the discrepancy in boiler structure, fuel properties, and operating conditions. In addition, a sensitivity analysis is carried out focusing on model parameters. Results show that some chemical kinetics and parameters about gas-solid two-phase flow significantly impact the NO_x emission for CFB combustion, such as the proportion of volatile-N in total fuel-N, kinetics about char reactions, gas flow distribution between phases, bubble

511 size, secondary air penetration depth, etc. However, the NO_x emission seems insensitive to the particle

512 external gas mass transfer coefficients.

513 This model provides a good starting point for further analyzing the CFB combustion

514 characteristics and minimizing the pollution emissions through operation optimization. In addition,

515 future studies can consider carrying out elaborate experiments or more detailed calculations to

516 validate the sub-models and assumptions applied in this paper. More field test data collected in large-

517 scale commercial CFB combustors are also necessary to improve the reliability of the integral CFB

518 combustion model.

519 **Nomenclature**

Abbreviation

CFB	circulating fluidized bed	PAPSD	primary ash particle size distribution
SA	secondary air	SCCS	static combustion and cold sieving

Symbols

A	cross-sectional area (m^2)	$A_{S,b}$ / $A_{S,f}$	heating surface areas at flue gas side / working medium side (m^2)
C_g	gas concentration (kmol·s^{-1})	$C_{g,\infty}$ / $C_{g,S}$	gas concentration in ambience / particle surface (kmol·s^{-1})
D_e	effective pore diffusion coefficient (m^2·s^{-1})	D_g	molecular diffusivity of gas (m^2·s^{-1})
d_p	particle size (m)	d_{cl}	cluster diameter in core region (m)
d_B	bubble diameter (m)	$d_{SA,in}$	diameter of SA inlet (m)
d_{fur}	equivalent diameter of furnace (m)	f	mass fraction of particles in cell (-)
f_s	roughness factor for solids (-)	G'	group reaction number (-)
H	height (m)	$H_{SA,J}$	height of SA influencing area (m)
H_{Dj}	penetration depth of jet from air distributor (m)	H_{Bj}	Length of jets induced by bubble breakage (m)
h	sensible enthalpy (kJ·kg^{-1}, kJ·kmol^{-1})	k	chemical reaction rate constant
K_h	total heat transfer coefficient (W·m^{-2}·K^{-1})	K_b^n	nominal heat transfer coefficient from bed to wall (W·m^{-2}·K^{-1})
K_f	heat transfer coefficient at working medium side (W·m^{-2}·K^{-1})	K_c	heat transfer coefficient of contamination over heating surface (W·m^{-2}·K^{-1})
K_g	mass transfer coefficient (m·s^{-1})	$l_{SA,pene}$	SA penetration depth (m)
M_s	mass holdup (kg)	MW	molar mass (kg·kmol^{-1})
$\dot{m}$	mass flux (kg·s^{-1}, kmol·s^{-1})	$\dot{m}_{g,in}$	injected gas flow rate (including fresh air and volatiles) (kmol·s^{-1})
$\dot{m}_{g,tran}$	interphase gas transport (kmol·s^{-1})	$\dot{m}_{O_2,SA}$	total oxygen inflow rate by SA (kmol·s^{-1})
Q	heat flow (kJ·s^{-1})	Q_{hs}	heat adsorbed by heating surface (kJ·s^{-1})
Q_r	heat released/consumed by chemical reactions (kJ·s^{-1})	R	chemical reaction rate (kmol·s^{-1}, kmol·m^{-3}·s^{-1}, kg·s^{-1})

r	particle radius (m)	Sh	Sherwood number
S_B	surface area of bubbles (m^2)	$S_{V,p}$	surface area of active particles per unit volume (m^{-1})
$s_{CaO,e}$ / $s_{CaO,ini}$	effective specific area / initial specific area of lime particle (m^2·kg^{-1})	T	temperature (K)
t	time (s)	U_g / U_{sg}	gas velocity / superficial gas velocity (m·s^{-1})
$\bar{U}_g$	mean gas velocity across furnace (m·s^{-1})	$U_{g,SA}$	SA injection velocity (m·s^{-1})
U_p / U_{sp}	particle velocity / superficial particle velocity (m·s^{-1})	$\bar{U}_p$	mean particle velocity across furnace (m·s^{-1})
U_{ss}	superficial slip velocity (m·s^{-1})	U_t	particle terminal velocity (m·s^{-1})
W	total solids/gas flow rate across furnace (kg·s^{-1}, kmol·s^{-1})	X_{CaO}	sulphation conversion rate of lime particle (-)
y_{feed}	primary particle size distribution (-)		

Greek symbols

α	molar ratio	β_{cl}	cluster fraction in core region (-)
γ	recombination efficiency of radical	δ_a	thickness of annulus (m)
δ_{fin} / δ_r	the thicknesses of fin / refractory castable (m)	Δ	difference
ε	bed voidage (-)	ξ	segregation index (-)
η_{cyc}	cyclone separation efficiency (-)	η_{eff}	effective reaction coefficient of near-wall active particles (-)
η_p	effectiveness factor for interparticle diffusion (-)	λ_{fin} / λ_r	heat conductivities of steel cylinder / refractory castable (W·m^{-1}·K^{-1})
μ	dynamic viscosity (Pa·s)	ρ	density (kg·m^{-3})
σ	volume fraction (-)	Φ_p	Thiele modulus of spherical particle (-)
Ψ	particle axial distribution (-)	$\Omega_{S/V}$	collision cross section per unit volume (m^{-1})

Subscripts

a / c	annular region / core region (upper zones)	abra	particle abrasion
ar	in received basis	cyc	cyclone
den	dense bed	down	downward solid materials
drain	discharge of bottom solid materials	E / B	emulsion phase / bubble phase (bubbling bed)
J / S	bubble jet center / jet surroundings (splash zone)	f / cl	dilute phase zone / cluster (core region in upper zones)
feed	input solids/gas/heat	fines	fine particles generated by abrasion
fur	furnace	fly	escaped solid materials
g	gas phase	i	cell
j	particle group	k	particle age group
m	chemical component	mf	minimum fluidization state
p	particle	r	chemical reaction
redu	particle reduction	RE	re-circulating solid materials
s	solid bed materials	sin	single particle
shift	particle attrition	up	upward solids/gas

Acknowledgment

References

[1] Yue G, Cai R, Lu J, Zhang H. From a CFB reactor to a CFB boiler – The review of R&D progress of CFB coal combustion technology in China, Powder Technol 2017; 316: 18-28.

[2] Leckner B. Fluidized bed combustion: mixing and pollutant limitation, Prog. Energy Combust. Sci. 1998; 24: 31-61.

[3] Glarborg P. Fuel nitrogen conversion in solid fuel fired systems, Prog. Energy Combust. Sci. 2003; 29: 89-113.

[4] Thomas KM. The release of nirogen oxides during char combustion, Fuel 1997; 76: 457-473.

[5] Johnsson JE. Formation and reduction of nitrogen oxides in fluidized-bed combustion, Fuel 1994; 73: 1398-1415.

[6] Li PW, Chyang CS, Ni HW. An experimental study of the effect of nitrogen origin on the formation and reduction of NO_x in fluidized-bed combustion, Energy 2018; 154: 319-327.

[7] Shahzad K, Saleem M, Ghauri M, Akhtar J, Ali N, Akhtar NA. Emissions of NO_x, SO_2, and CO from co-combustion of wheat straw and coal under fast fluidized bed condition, Combust Sci Technol 2014; 187: 1079-1092.

[8] Lupiáñez C, Guedea I, Bolea I, Díez LI, Romeo LM. Experimental study of SO_2 and NO_x emissions in fluidized bed oxy-fuel combustion, Fuel Process Technol 2013; 106: 587-594.

[9] Qi G, Zhang S, Liu X, Guan J, Chang Y, Wang Z. Combustion adjustment test of circulating fluidized bed boiler, Appl Therm Eng 2017; 124: 1505-1511.

[10] Wang XS, Gibbs BM, Rhodes MJ. Impact of air staging on the fate of NO and N_2O in a circulating fluidized-bed combustor, Combust Flame 1994; 99: 508-515.

[11] Tourunen A, Saastamoinen J, Nevalainen H. Experimental trends of NO in circulating fluidized bed combustion, Fuel 2009; 88: 1333-1341.

[12] Diego LFd, Londono CA, Wang XS, Gibbs BM. Influence of operating parameters on NO_x and N_2O axial profiles in a circulating fluidized bed combustor, Fuel 1996; 75: 971-978.

[13] Zhao J, Grace JR, Lim CJ, Brereton CMH, Legros R. Influence of operating parameters on NO_x emissions from a circulating fluidized bed combustor, Fuel 1994, 73: 1650-1657.

[14] Ke X, Cai R, Zhang M, Miao M, Lyu J, Yang H. Application of ultra-low NO_x emission control for CFB boilers based on theoretical analysis and industrial practices, Fuel Process Technol 2018; 181: 252-258.

[15] Xu L, Cheng L, Ji J, Wang Q, Fang M. A comprehensive CFD combustion model for supercritical CFB boilers, Particuology 2019; 43: 29-37.

[16] Xie J, Zhong W, Shao Y, Liu Q, Liu L, Liu G. Simulation of combustion of municipal solid waste and coal in an industrial-scale circulating fluidized bed boiler, Energ Fuel 2017; 31: 14248-14261.

[17] Zhou W, Zhao C, Duan L, Chen X, Liang C. Two-dimensional computational fluid dynamics simulation of nitrogen and sulfur oxides emissions in a circulating fluidized bed combustor, Chem Eng J 2011; 173: 564-573.

[18] Selcuk N, Ozkan M. Simulation of circulating fluidized bed combustors firing indigenous lignite, Int J Therm Sci 201; 50: 1109-1115.

[19] Krzywanski J, Czakiert T, Muskala W, Sekret R, Nowak W. Modeling of solid fuels combustion in oxygen-enriched atmosphere in circulating fluidized bed boiler: Part 1. The mathematical model of fuel combustion in oxygen-enriched CFB environment, Fuel Process Technol 2010; 91: 290-295.

[20] Gungor A. Simulation of NO_x emission in circulating fluidized beds burning low-grade fuels, Energ Fuel 2009; 23: 2475–2481.

[21] Coda Zabetta E, Hupa M. A detailed kinetic mechanism including methanol and nitrogen pollutants relevant to the gas-phase combustion and pyrolysis of biomass-derived fuels, Combust Flame 2008; 152: 14-27.

[22] Giménez-López J, Millera A, Bilbao R, Alzueta MU. HCN oxidation in an O_2/CO_2 atmosphere: An experimental and kinetic modeling study, Combust Flame 2010; 157: 267-276.

[23] Dagaut P, Glarborg P, Alzueta M. The oxidation of hydrogen cyanide and related chemistry, Prog. Energy Combust. Sci. 2008; 34: 1-46.

[24] Kilpinen P, Kallio S, Konttinen J, Mueller C, Jungar A, Hupa M, et al. Towards a quantitatitive understanding of NO_x and N_2O emission formation in full-scale circulating fluidised bed combustors, 16th International Conference on Fluidized Bed Combustion, 2001.

[25] Li Y, Lu G, Rudolph V. The kinetics of NO and N_2O reduction over coal chars in fluidised-bed combustion, Chem Eng Sci 1998; 53: 1-26.

[26] Hayhurst AN, Lawrence AD. The reduction of the nitrogen oxides NO and N_2O to molecular nitrogen in the presence of iron, its oxides, and carbon monoxide in a hot fluidized bed, Combust Flame 1997; 110: 351-365.

[27] Garijo EG, Jensen AD, Glarborg P. Reactivity of coal char in reducing NO, Combust Flame 2004; 136: 249-253.

[28] Hayhurst AN, Lawrence AD. The effect of solid CaO on the production of NO_x and N_2O in fluidized bed combustors: Studies using pyridine as a prototypical nitrogenous fuel, Combust Flame 1996; 105: 511-527.

[29] Lupiáñez C, Díez LI, Romeo LM. NO emissions from anthracite oxy-firing in a fluidized-bed combustor: Effect of the temperature, limestone, and O_2, Energ Fuel 2013; 27: 7619-7627.

[30] Hayhurst AN, Parmar MS. Measurement of the mass transfer coefficient and sherwood number for carbon spheres burning in a bubbling fluidized bed, Combust Flame 2002; 130: 361-375.

[31] Hou B, Tang H, Zhang H, Shao G, Li H, Zhu Q. Experimental and theoretical investigation of mass transfer in a circulating fluidized bed, Chem Eng Sci 2013; 102: 354-364.

[32] Dennis JS, Hayhurst AN, Scott SA. The combustion of large particles of char in bubbling fluidized beds: The dependence of Sherwood number and the rate of burning on particle diameter, Combust Flame 2006; 147: 185-194.

[33] He W, Liu Y, He R, Ito T, Suda T, Fujimori T, et al. Combustion rate for char with fractal pore characteristics, Combust Sci Technol 2013; 185: 1624-1643.

[34] Lundberg L, Pallarès D, Thunman H. Upscaling effects on char conversion in dual fluidized bed gasification, Energ Fuel 2018; 32: 5933-5943.

[35] Blaszczuk A, Zylka A, Leszczynski J. Simulation of mass balance behavior in a large-scale circulating fluidized bed reactor, Particuology 2016; 25: 51-58.

[36] Liu X, Zhang M, Lu J, Yang H. Effect of furnace pressure drop on heat transfer in a 135MW CFB boiler, Powder Technol 2015, 284: 19-24.

[37] Paulus HJ. Mathematical modelling of circulating fluidized bed combustion. Delft University of Technology, 1998.

[38] Cai R, Zhang H, Zhang M, Yang H, Lyu J, Yue G. Development and application of the design principle of fluidization state specification in CFB coal combustion, Fuel Process Technol 2018; 174: 41-52.

[39] Leckner B. Regimes of large-scale fluidized beds for solid fuel conversion, Powder Technol 2017; 308: 362-367.

[40] Basu P. Circulating fluidized bed boilers design operation and maintenance, Springer Press, 2015.

[41] Haus J, Hartge E-U, Heinrich S, Werther J. Dynamic flowsheet simulation for chemical looping combustion of methane, Int J Greenh Gas Con 2018; 72: 26-37.

[42] Gungor A. Prediction of SO_2 and NO_x emissions for low-grade Turkish lignites in CFB combustors, Chem Eng J 2009; 146: 388-400.

[43] Xu H, Ma J, Zhao H. Macroscopic fuel reactor modelling of a $5\,kW_{th}$ interconnected fluidized bed for in-situ gasification chemical looping combustion of coal, Chem Eng J 2018; 348: 978-991.

[44] Chen C, Dai Q. Qi H. Improvement of EMMS drag model for heterogeneous gas–solid flows based on cluster modeling, Chem Eng Sci 2016; 141: 8-16.

[45] Zhang M, Zhang C. A type-A-choking-oriented unified model for fast fluidization dynamics, Powder Technol 2013, 241:126-141.

[46] Prajongkan Y, Piumsomboon P, Chalermsinsuwan B. Computation of mass transfer coefficient and Sherwood number in circulating fluidized bed downer using computational fluid dynamics simulation, Chem Eng Process 2012; 59: 22-35.

[47] Lyngfelt A, Amand L-E, Leckner B. Progress of combustion in the furnace of a circulating fluidized bed boiler, Twenty-Sixth Symposium (International) on Combustion, 26 (1996) 3253–3259.

[48] Yan J, Lu X, Wang Q, Kang Y, Li J, Xu Z, et al. Study on the influence of secondary air on the distributions of flue gas composition at the lower part of a 600 MW supercritical CFB boiler, Fuel Process Technol 2019; 196: 106035.

[49] Koeninger B, Hensler T, Schug S, Arlt W, Wirth K-E. Horizontal secondary gas injection in fluidized beds: Solid concentration and velocity in multiphase jets, Powder Technol 2017; 316: 49-58.

[50] Cui H, Mostoufi N, Chaouki J. Characterization of dynamic gas–solid distribution in fluidized beds, Chem Eng J 2000; 79: 133-143.

[51] Cloete JH, Cloete S, Radl S, Amini S. Evaluation of wall friction models for riser flow, Powder Technol 2016; 303: 156-167.

[52] Xu G, Sun G, Gao S. Estimating radial voidage profiles for all fluidization regimes in circulating fluidized bed risers, Powder Technol 2004; 139: 186-192.

[53] Harris AT, Davidson JF, Thorpe RB. The prediction of particle cluster properties in the near wall region of a vertical riser, Powder Technol 2002; 127: 128-143.

[54] Dai Q, Chen C, Qi H. Influence of meso-scale structures on drag in gas–solid fluidized beds, Powder Technol 2016; 288: 87-95.

[55] Zhou X, Xie J, Gao S, Fan Y, Cheng L, Chen K. Measurement of solid flux distribution near water wall of a 330 MW CFB boiler, Chin J Power Eng 2014; 34: 753-758.

[56] Bai D, Zhu J, Jin Y, Yu Z. Internal recirculation flow structure in vertical upflow gas-solid suspensions Part II. Flow structure predictions, Powder Technol 1995; 85: 179-188.

[57] Ke X, Engblom M, Zhang M, Silva PSPd, Hupa L, Lyu J, et al. Modeling of the axial distributions of volatile species in a CFB boiler, Chem Eng Sci 2020; 233: 116436.

[58] Ke X, Li D, Cai R, Lyu J, Yang H, Zhang M, et al. 1-Dimensional modelling of in-situ desulphurization performance of a 550 MW_e ultra-supercritical CFB boiler, Fuel 2020; 290: 120088.

[59] Ke X, Li D, Zhang M, Jeon C-H, Cai R, Cai J, et al. Ash formation characteristics of two Indonesian coals and the change of ash properties with particle size, Fuel Process Technol 2019; 186: 73-80.

[60] Li S. Researches on post combustion in the cyclone of circulating fluidized bed boiler. Tsinghua University, 2009.

[61] Paprika M, Komatina M, Dakić D, Živković G, Mladenović M. Experimental and numerical investigation of the primary fragmentation of a lignite during fluidized-bed (FB) devolatilization, Energ Fuel 2015; 29: 3394-3398.

[62] Bai D, Zhu J, Jin Y, Yu Z. Internal recirculation flow structure in vertical upflow gas-solids suspensions Part I. A core-annulus model, Powder Technol 1995; 85: 171-177.

[63] Laarhoven PJMv, Aarts EHL. Simulated annealing: Theory and applications, Springer, Dordrecht, 1987.

[64] Li J, Kwauk M. Exploring complex systems in chemical engineering - the multi-scale methodology, Chem Eng Sci 2003; 58: 521-535.

[65] Ge W, Li J. Physical mapping of fuidization regimes - the EMMS approach, Chem Eng Sci 2002; 57: 3993-4004.

[66] Ke X, Engblom M, Cheng L, Chen L, Cai R, Hupa L, et al. Modeling and experimental investigation on the fuel particle heat-up and devolatilization behavior in a fluidized bed, Fuel 2021; 288: 119794.

[67] Phiri Z, Everson RC, Neomagus HWJP, Engelbrecht AD, Wood BJ, Nyangwa B. Release of nitrogenous volatile species from South African bituminous coals during pyrolysis, Energ Fuel 2018; 32: 4606-4616.

[68] Becidan M, Skreiberg Ø, Hustad JE. NO_x and N_2O precursors (NH_3 and HCN) in pyrolysis of biomass residues, Energ Fuel 2007; 21: 1173-1180.

[69] Leppalahti J, Koljonen T. Nitrogen evolution from coal, peat and wood during gasification: Literature review, Fuel Process Technol 1995; 43: 1-45.

652   [70] Zhang H, Fletcher TH. Nitrogen transformations during secondary coal pyrolysis, Energ Fuel 2001; 15: 1512-1522.

653   [71] Lutz AE, Kee RJ, Miller JA. SENKIN: A Fortran program for predicting homogeneous gas phase chemical kinetics with
654   sensitivity analysis, United States, 1988.

655   [72] Loeffler G, Hofbauer H. Does CO burn in a fluidized bed? - A detailed chemical kinetic modeling study, Combust Flame 2002;
656   129: 439-452.

657   [73] Kim YC, Boudart M. Recombination of oxygen, nitrogen, and hydrogen atoms on silica: kinetics and mechanism, Langmuir 1991;
658   7: 2999-3005.

659   [74] Fu S, Song Q, Tang J, Yao Q. Effect of CaO on the selective non-catalytic reduction deNOx process: Experimental and kinetic
660   study, Chem Eng J 2014; 249: 252-259.

661   [75] Sit SP, Grace JR. Effect of bubble interaction on interphase mass transfer in gas fluidized beds, Chem Eng Sci 1981; 36: 327-335.

662   [76] Scala F. Mass transfer around freely moving active particles in the dense phase of a gas fluidized bed of inert particles, Chem Eng
663   Sci 2007; 62: 4159-4176.

664   [77] Annamalai K, Ryan W. Interactive processes in gasification and combustion, part 2: isolated carbon, coal and porous char
665   particles, Prog. Energy Combust. Sci. 1993; 19: 383-446.

666   [78] Annamalai K, Ramalingam SC. Group combustion of char carbon particles, Combust Flame 1987; 70: 307-332.

667   [79] Li S, Yang H, Zhang H, Wu Y, Lyu J, Yue G. Combustion model for a CFB boiler with consideration of post-combustion in the
668   cyclone, 20th International Conference on Fluidized Bed Combustion 2009: 824-828.

669   [80] Yang J, Yang H, Yue G. Experimental study on secondary air jet penetration in circulating fluidized bed, J Power Eng 2008; 28:
670   509-513.

671   [81] Wang P. Study on secondary air injection and solids dispersion in the splash zone of a circulating fluidized bed, Tsinghua
672   University, 2017.

673   [82] Lu J, Zhang J, Yue G, Liu Q, Yu L, Lin X, et al. Method of calculation of heat transfer coefficient of the heater in a circulating
674   fluidized bed furnace, Heat Transfer-Asian Research 2002; 31: 540-550.

675   [83] Ke X, Cai R, Yang H, Zhang M, Zhang H, Wu Y, et al. Formation and ultra-low emission of NO_x for circulating fluidized bed
676   combustion, Proceedings of the CSEE 2018; 38(2): 390-396.

677   [84] Knobig T, Werther J, Åmand L-E, Leckner B. Comparison of large- and small-scale circulating fluidized bed combustors with
678   respect to pollutant formation and reduction for different fuels, Fuel 1998; 77: 1635-1642.

679   [85] Åmand L-E, Andersson S. Emissions of nitrous oxide (N_2O) from fluidized bed boilers, Proceedings of the 10th International
680   Conference on Fluidized Bed Combustion 1989; 49-56.